Bulletin of the Seismological Society of America, Vol. 107, No. 2, pp. –, April 2017, doi: 10.1785/0120160262

Ⓔ

An Assessment of Crustal and Upper-Mantle Velocity Structure by Removing the Effect of an Ice Layer on the *P*-Wave Response: An Application to Antarctic Seismic Studies

by Jordan H. Graw, Samantha E. Hansen, Charles A. Langston, Brian A. Young, Akram Mostafanejad, and Yongcheol Park

Abstract Standard *P*-wave receiver function analyses in polar environments can be difficult because reverberations in thick ice coverage often mask important *P*-to-*S* conversions from deeper subsurface structure and increase ambient noise levels, thereby significantly decreasing the signal-to-noise ratio of the data. In this study, we present an alternative approach to image the subsurface structure beneath ice sheets. We utilize downward continuation and wavefield decomposition of the *P*-wave response to obtain the up- and downgoing *P* and *S* wavefield potentials, which removes the effects of the ice sheet. The upgoing *P* wavefield, computed from decomposition of the waveform at a reference depth, is capable of indicating ice layer thickness. This simple step removes the necessity of modeling ice layer effects during iterative inversions and hastens the overall velocity analysis needed for downward continuation. The upgoing *S* wave is employed and modeled using standard inversion techniques as is done with receiver functions at the free surface using a least-squares approximation. To illustrate our proof of concept, data from several Antarctic networks are examined, and our results are compared with those from previous investigations using *P*- and *S*-wave receiver functions as well as body- and surface-wave tomographic analyses. We demonstrate how our approach satisfactorily removes the ice layer, thus creating a dataset that can be modeled for crustal and upper-mantle structure. Solution models indicate crustal thicknesses as well as average crustal and upper-mantle shear-wave velocities.

Electronic Supplement: Figure of measured data, the vertical-component stack used in deconvolution, and the resultant vertical, radial, and tangential transfer functions.

Introduction

Teleseismic *P* waves fundamentally contain information related to earthquake source time functions, heterogeneities along the path of propagation, and near-receiver subsurface structure. It is because of this that *P*-wave receiver functions (PRFs) and transfer functions are so widely adopted to study the Earth structure beneath a given station. In receiver function analysis, the vertical component of motion is deconvolved from the corresponding horizontal component to identify converted signals from seismic discontinuities in the subsurface; however, in the case of transfer functions, a network-averaged vertical component is instead used for deconvolution. As a result, standard PRFs only contain *P*-to-*S* (*Ps*) conversions, whereas transfer functions contain both *Ps* conversions as well as *P*-wave reverberations, thus containing more information about the subsurface.

A substantial limitation to either approach lies within the terminus of the propagation path. Specifically, if near-surface low-velocity layers are present, reverberations produced within these layers can mask phase conversions from deeper discontinuities, making it difficult, if not impossible, to analyze the conversions of interest (Kumar *et al.*, 2005; Hansen *et al.*, 2009, 2010, 2016; Langston, 2011; Chaput *et al.*, 2014). This is particularly an issue in polar environments, where thick ice sheets at the surface have compressional (V_P; km s^{-1}) and shear-wave (V_S; km s^{-1}) velocities that are much lower than typical crustal rocks and thus introduce large impedance contrasts between the free surface and the geologic basement. Seismic energy becomes trapped by the lower seismic velocities of the ice layer, leading to reverberations and increased high amplitude noise, reducing the signal-to-noise ratio (SNR) of the data compared to stations

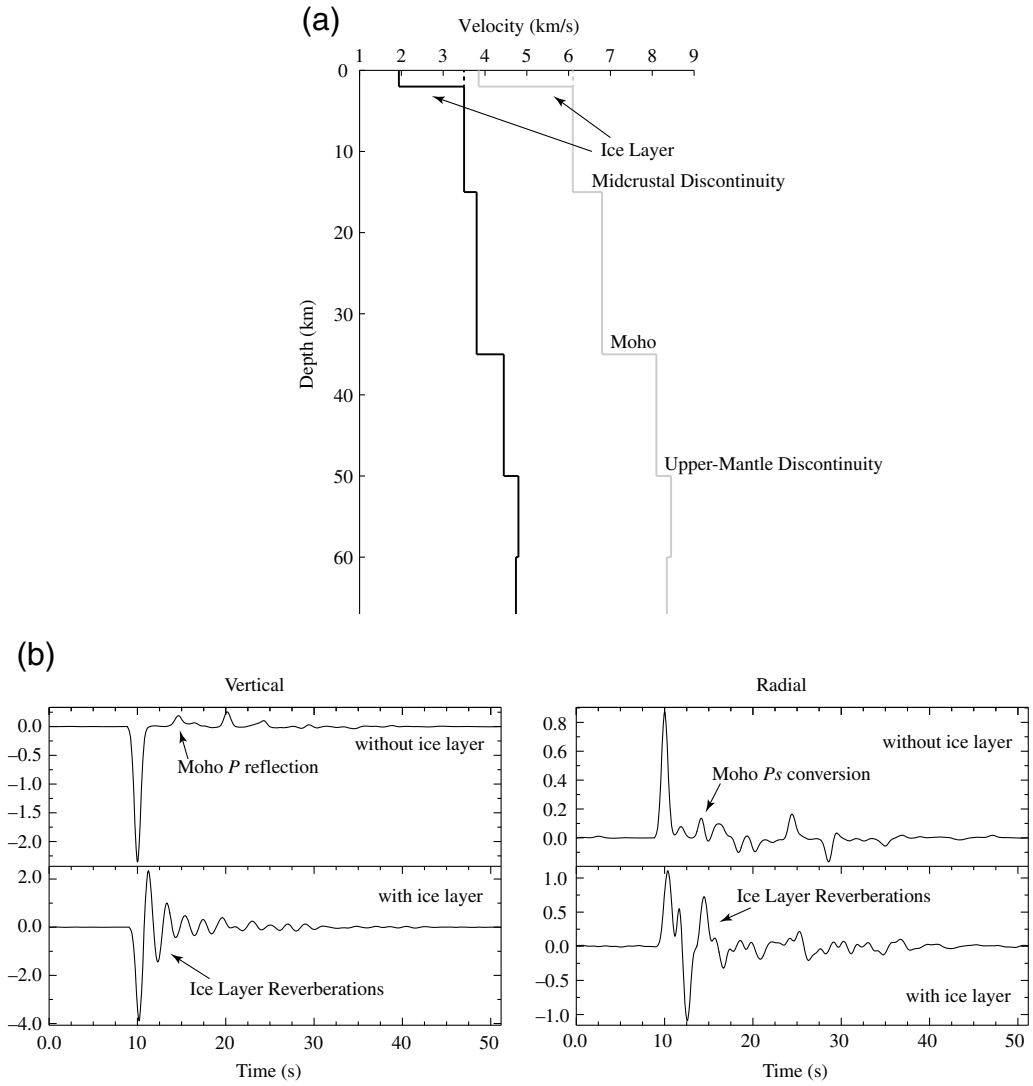

Figure 1. Synthetic examples illustrating the effects of an ice layer. Synthetic seismograms were created using a Haskell propagator matrix formulation without attenuation effects (Haskell, 1962). The frequency content of all synthetics is ~1 Hz. (a) Model (solid lines) used to create the synthetic data, in which the ice layer is 2.0 km thick. The black line is shear-wave velocity, and the gray line is compressional-wave velocity. Dashed lines indicate a comparable model with no ice layer. (b) Synthetic (left) vertical- and (right) radial-component transfer functions. (Top) Synthetic seismograms using the velocity model in (a), without the ice layer. Phase conversions are identifiable within the traces. (Bottom) Synthetic seismograms using the velocity model in (a), with the 2.0-km-thick ice layer. The ice reverberations are clearly seen in both the vertical and radial signals, masking phase conversions of interest.

on hard rock. Such effects are illustrated with synthetic examples in Figure 1. The presence of a thin surficial ice layer causes both the radial and vertical-component transfer functions to be dominated by reverberations, and the *Ps* conversion from the crust–mantle boundary (Moho) becomes irresolvable.

Different approaches have been taken to model subsurface structure beneath ice layers. One relatively new method computes *S*-wave receiver functions (SRFs; Hansen *et al.*, 2009, 2010, 2016), in which the radial component of motion is deconvolved from the vertical component to model *S*-to-*P* (*Sp*) phase conversions from seismic discontinuities. Unlike the *Ps* conversions within a PRF, which arrive at the same time as reverberations created by an ice layer, *Sp* conversions within an SRF are unaffected by the ice layer because they arrive before the direct *S* wave and the reverberations, making them well-suited to image crustal thickness. However, this method does not come without its limitations. SRFs often contain high levels of noise because the signals of interest arrive within the direct *P*-wave coda. Additionally, they contain lower frequency signals compared to PRFs, resulting in receiver functions with lower resolution. This inhibits their ability to resolve thin layers within the subsurface. Alternative approaches have instead still tried to employ PRFs to image subsurface structure, despite the issues noted above. In these cases, the near-surface structure (i.e., the ice layer) must first be modeled and then applied to each successive iteration of inversions used to model the Earth structure. Chaput *et al.* (2014), for instance, were able to use PRFs from

stations deployed on the West Antarctic ice sheet to image crustal structure by forward modeling the amplitude of the ice signatures within their dataset. This approach requires extensive analysis to simultaneously solve for both ice and the Earth structure, and although Chaput *et al.* (2014) were able to image the subsurface beneath their study area, their approach required them to favor solution models with low numbers of discontinuities because the large amplitude ice layer reverberations caused unrealistic jumps from low to high velocities within their models. To calculate smoother, more realistic models, they had to sacrifice resolution of small-scale discontinuities in the crust and/or upper mantle.

Here, we present a more direct approach to assess subsurface structure beneath seismic stations situated on ice. Using downward continuation and wavefield decomposition, we are able to remove the effects of an ice layer. Our methodology builds on that of Langston (2011), who used a similar approach to assess the effects of low-velocity surface sediments on transfer functions recorded by stations in the Mississippi embayment. Although this approach proved to be successful at removing the effects of unconsolidated sediments from transfer functions, it is untested for ice sheets and presents a new analysis technique for polar environments. Further, our study illustrates how the upgoing *S* wavefield potential, which is calculated by decomposing the downward-continued transfer function, can be inverted for the Earth structure beneath a given station. Downward continuation and wavefield decomposition require that the thickness of the ice sheet be known, but this parameter is readily calculated using our approach. The upgoing *S*-wave potential at depth is modeled, thereby eliminating the need for the ice layer in each iteration. We applied our method to datasets from Antarctica and find crustal thicknesses as well as average crustal and upper-mantle shear-wave velocities that agree with those from previous studies. This illustrates that our method is capable of calculating crustal and upper-mantle structure without the need to oversimplify the solution models and without seemingly large uncertainties associated with the structure therein.

Synthetic Seismogram Analysis

Downward Continuation and Wavefield Decomposition

To demonstrate the robustness of our methodology, we will first examine synthetic data, using the same vertical and radial components shown in Figure 1. The corresponding, noise-free synthetic seismograms were created using a Haskell propagator matrix formulation (Haskell, 1962). A ray parameter of 0.06 s/km was used because this is a typical value associated with the average distance of teleseismic data used in receiver function analyses (corresponding to ~60° epicentral distance, in this case).

We employ the method of Langston (2011), in which the vertical- and radial-component transfer functions are downward continued, or relocated beneath the ice sheet, using a propagator matrix for the *P*-to-*SV* (*P-SV*) system. The transfer functions are then decomposed into their respective up- and downgoing *P*- and *S*-wave potentials. The downgoing *P* wavefield is primarily composed of free-surface reflections and near-surface ice layer reverberations, which have large amplitudes and complex waveforms. The downgoing *S* wavefield contains *Ps* conversions and reverberations from both the ice layer and the free surface. The upgoing *P* wavefield shows secondary reflections and *Sp* conversions from interfaces below the depth that has been downward continued to, and this field plays an important role in determining ice layer thickness, which will be discussed further below. Finally, the upgoing *S* wavefield contains *Ps* conversions from deeper crustal and upper-mantle discontinuities. Given this, the upgoing *S* wavefield contains the best information for the Earth structure, containing the *Ps* conversions needed for modeling, and hence it is the primary focus of this method.

The velocity structure and thickness of the surface medium through which the *P* and *S* waves are being downward continued must be known. Langston (2011) developed a grid-search algorithm to find the best velocity model for his study area; however, ice is a much simpler medium compared to sediment. Although seismic properties within ice are dependent on temperature, the variations in observed velocity are negligible, varying by only ± 0.02 km s^{-1} (Kohnen, 1974). A very low-velocity firn layer, up to 100 m thick, exists over much of the Antarctic ice sheet, and because the velocity employed in travel-time calculations is the root mean square (rms) velocity, the effect of the firn layer would be amplified where the ice layer is thin (< 1 km). For stations situated on such thin ice layers, accurate velocity analysis would require the thickness of the firn layer to be known, possibly from ground-penetrating radar measurements. However, most seismic stations in Antarctica deployed on ice are underlain by a substantially thick ice layer (> 1 km), where the firn effects are less influential. Therefore, we assume an average V_P of 3.84 km s^{-1} and an average V_S of 1.94 km s^{-1} for the ice layer in our model (Kohnen, 1974).

A more problematic aspect to polar investigations is determining the thickness of the ice layer. Satellite- and airborne-derived ice thickness measurements are available for some polar locations (e.g., Fretwell *et al.*, 2013), but these datasets often do not provide coverage of remote areas. As stated above, the upgoing *P* wavefield can be readily employed to calculate this parameter. By generating multiple velocity models, each with the same subsurface structure but with different ice layer thicknesses, we are able to downward continue and decompose the *P*-wave response at a depth just below each model's ice layer to determine the upgoing *P* wave potential for each model. Because the upgoing *P* wavefield contains secondary reflections, we can identify the trace that displays the least reverberations. Figure 2 shows the results of such an assessment by plotting each successive upgoing *P* wavefield for each tested model, for which the ice thickness is incrementally increased by 100 m. The model used to create the synthetic seismograms (Fig. 1) included a 2.0-km-thick ice layer. The upgoing *P* wave-

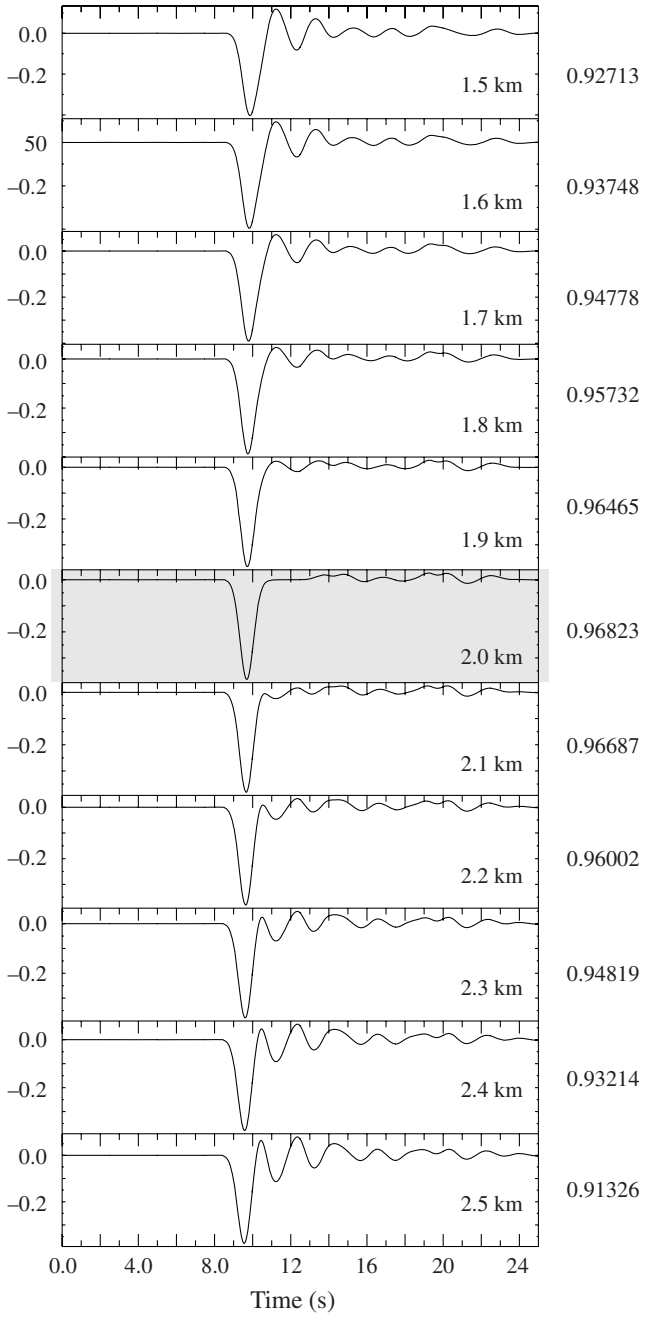

Figure 2. Upgoing *P* wavefields for a series of downward-continuation and wavefield-decomposition analyses to identify ice thickness. Identical velocity models were used for each successive run, except the ice layer thickness was varied from 1.5 to 2.5 km in 0.1 km increments. Correlation coefficients are displayed to the right of each wavefield. Gray shading highlights the model with 2.0-km-thick ice, matching the model in Figure 1. This trace displays the clearest waveform, with minimal secondary reflections, and the highest correlation coefficient.

fields from models with an ice layer thinner than 2.0 km show secondary reflections and indicate that the downward-continued data are still within the ice layer. In contrast, traces from models with ice layers thicker than 2.0 km indicate that downward continuation has exceeded a depth where the Earth structure is known. That is, the data cannot reconcile incorrect velocity analysis with information contained within the waveform, again leading to secondary reflections. The upgoing *P* wavefield from the model with a 2.0-km-thick ice layer contains the least amount of reverberations, which coincides with the ice layer thickness in the true model, thereby indicating the correct ice thickness. We quantify the ice thickness test using a cross-correlation technique. This technique is performed for each upgoing *P* wave created previously. Each downward-continued and wavefield-decomposed upgoing *P* wave is individually cross correlated with the other downward-continued and wavefield-decomposed upgoing *P* waves. Then, the maximum correlation coefficient is found for each cross correlation. Finally, we take the average of the maximum correlation coefficients (Fig. 2). These steps allow us to assess which individual upgoing *P* wave is most similar to the entire group of upgoing *P* waves. The upgoing *P* wave that best indicates the thickness of the ice layer will have a quasi-impulse signature, or rather, it will have the least amount of reverberations, which will correlate best with the other upgoing *P* waves because the correlation will be primarily fitting the impulse rather than reverberations (Fig. 2). The resolution of the ice thickness is ~200 m, because the cross-correlation coefficients do not show a strong minimum. However, the high correlation coefficient value, combined with a visual inspection of the waveforms, indicates the correct thickness for the ice layer (Fig. 2).

The synthetic vertical and radial transfer functions shown in Figure 1 are downward continued to a depth of 2.05 km. The additional 50 m insures proper permeation through the ice layer but does not include enough unknown velocity structure to affect the waveform. The resultant upgoing *S* wavefield is shown in Figure 3, and it is the focus of further analysis.

Windowing the Upgoing S Wavefield

Selecting the correct window size for the upgoing *S* wavefield is a crucial step prior to inversion. The upgoing *S* wavefield contains various phases that can be directly modeled for the Earth structure, and depending on the depth of that structure beneath a given station, these phases arrive at various times. Although downward continuation is capable of removing reverberations from an ice layer that mask deeper *Ps* phases, reverberations from the ice layer return at later times in the upgoing *S* wavefield as reflections from lower crustal interfaces, ultimately masking deeper phase conversions. Therefore, a correct window length is important to minimize the reverberations included in the inversion. This is illustrated in Figure 4, in which synthetic seismograms have been downward continued to various depths, and the resulting upgoing *S* wavefields are plotted. Tests were performed with three input models, each essentially the same as that shown in Figure 1 but with a range of Moho depths at 20, 35, and 40 km. Ice layer reverberations are seen just after the arrival of the *Ps* reflection of the downgoing *P* wave at the Moho (S_{Moho}; Fig. 4). It is desirable to have some knowledge of the subsurface structure prior to windowing;

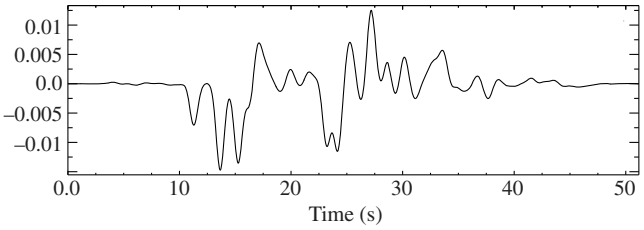

Figure 3. Synthetic upgoing *S* wavefield, constructed using the velocity model in Figure 1. The corresponding transfer functions (Fig. 1) were downward continued to a depth of 2.05 km, as described in the Downward Continuation and Wavefield Decomposition section.

however, this is not always possible. Through our windowing tests, we observe that the *Ps* reflection of the downgoing *P* wave at the Moho is a relatively large phase and can be readily identified within the upgoing *S* wavefield. Therefore, if no *a priori* information is available, we recommend windowing the upgoing *S* wavefield around the main phases of conversion, terminating after the *Ps* reflection of the downgoing *P* wave at the Moho, thereby removing the later ice layer reverberations. Given the assessment shown in Figure 4, we window the upgoing *S* wavefield (Fig. 3) from 0 to 25.57 s prior to inversion.

Inversion of the Upgoing *S* Wavefield

We developed an approach to invert the upgoing *S* wavefield for subsurface shear-wave velocity structure. The inversion is analogous to typical receiver function inversions at the free surface. Our least-squares technique follows the approach of Ammon *et al.* (1990), in which we calculate velocity values rather than velocity perturbations. To accomplish this, we use

$$\begin{bmatrix} \mathbf{D} \\ \sigma\mathbf{\Delta} \end{bmatrix}\mathbf{m} = \begin{bmatrix} \mathbf{d} \\ \mathbf{0} \end{bmatrix} + \begin{bmatrix} \mathbf{D} \\ \mathbf{0} \end{bmatrix}\mathbf{m}_0, \tag{1}$$

in which $\mathbf{D}$ is the m by n partial derivative matrix ($\partial R_i^{\text{syn}}/\partial m_k$) composed of synthetic upgoing *S* waves created by perturbations to each layer of the starting model $\mathbf{m}_0$. The elements of $\mathbf{D}$ represent the sensitivity of the ith synthetic waveform (R^{syn}) to a small perturbation in the kth layer of $\mathbf{m}_0$. m is the number of data points, n is the number of model parameters, $\mathbf{m}$ is the model, $\mathbf{d}$ is an $m \times 1$ residual vector, and σ is a multiplier that weights the second derivative matrix ($\mathbf{\Delta}$). For each iteration, we approximate V_P based on the corresponding value of V_S. We approximate V_P using equation (2) from Brocher (2005), in which

$$V_P(\text{km s}^{-1}) = 0.9409 + 2.0947V_S - 0.8206V_S^2 + 0.2683V_S^3 - 0.0251V_S^4. \tag{2}$$

This relationship is valid for V_S between 0 and 4.5 km s^{-1}. For V_S values ≥4.4 km s^{-1}, we approximate V_P using a V_P/V_S ratio of 1.8, which is typical at upper-mantle depths. We calculate density (ρ) using the Nafe–Drake curve, which is valid for V_P between 1.5 and 8.5 km s^{-1}:

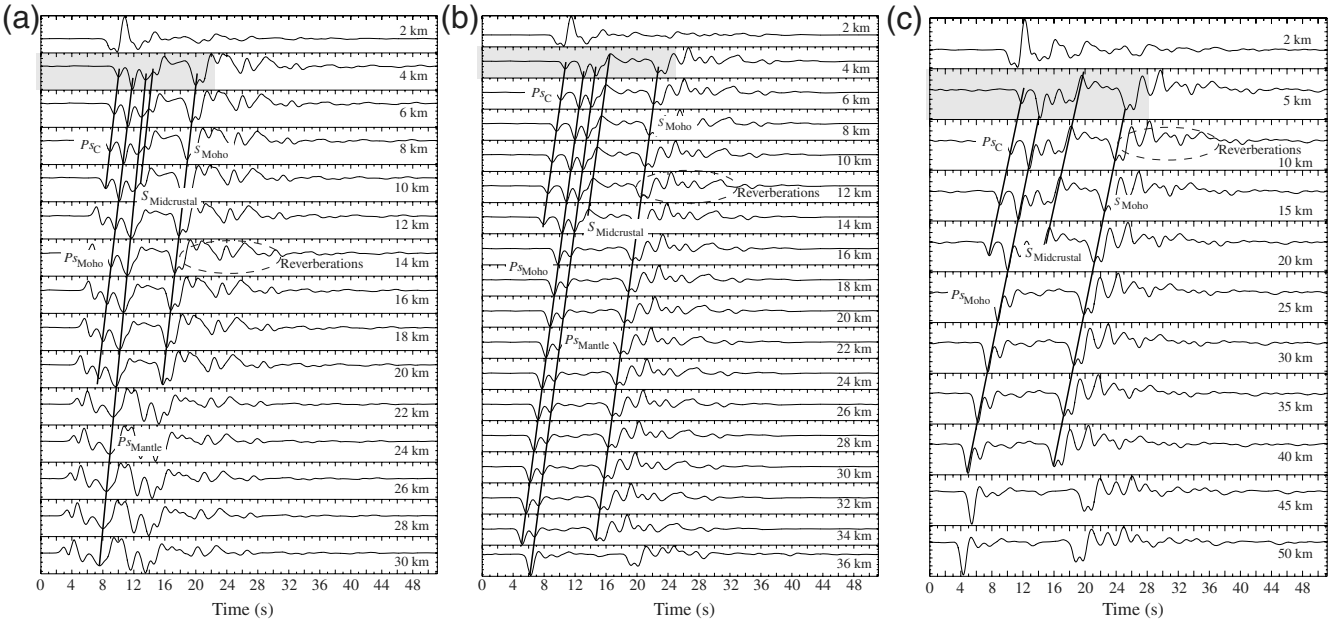

Figure 4. Tests to assess proper window length prior to inversion. Each test uses the vertical and radial transfer functions created with a 2.0-km-thick ice layer (Fig. 1), and downward continuation is performed using the model in Figure 1 but with various crustal thicknesses. (a) Crustal thickness of 20 km, (b) crustal thickness of 35 km, and (c) crustal thickness of 40 km. Each trace shows the upgoing *S* wavefield, with the corresponding downward-continuation depth displayed on the right. Phases terminate at their respective depths. Reverberations return after the S_{Moho} arrival in each test. The gray shading indicates the recommended window for each velocity model. Ps_c is the *Ps* conversion from the midcrustal velocity increase in Figure 1; Ps_{Moho} is the *Ps* conversion at the Moho; Ps_{Mantle} is the *Ps* conversion from the upper-mantle velocity increase shown in Figure 1; $S_{\text{Midcrustal}}$ is the *Ps* reflection from the midcrustal velocity increase in Figure 1; and S_{Moho} is the *Ps* reflection of the downgoing *P* wave at the Moho.

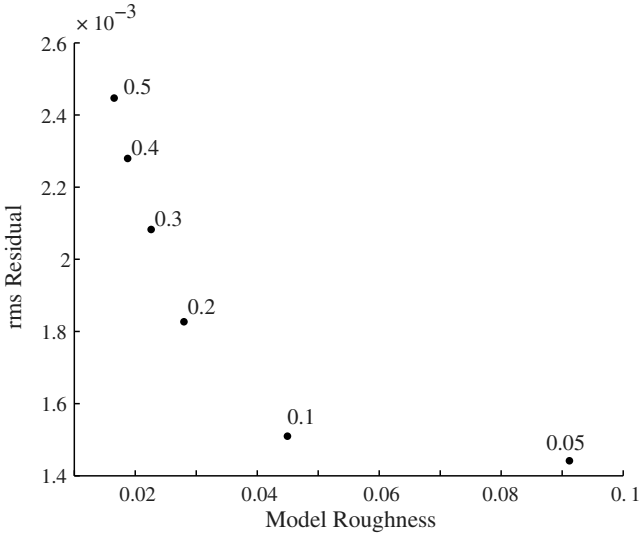

Figure 5. Plot showing the trade-off between waveform fit and model roughness. Smoothing parameter values are denoted next to each plotted point. Note that increasing the smoothing parameter creates both a smoother model but a poorer fit to the data. For the synthetic example, we choose a smoothing parameter for 0.1 for the inversion process because it reduces the residual vector while not oversmoothing the solution.

$$\rho(\mathrm{g/cm^3}) = 1.6612V_P - 0.4721V_P^2 + 0.0671V_P^3 - 0.0043V_P^4 + 0.000106V_P^5 \quad (3)$$

(Brocher, 2005).

Waveform fitting can be a difficult process because there is always a trade-off between model smoothness and detailed waveform fit. To address this issue, we run a suite of inversions with varying σ values to assess the trade-off between waveform fit and model roughness. Following the approach of Ammon *et al.* (1990), model roughness is calculated by

$$\text{Roughness} = \sum_{i=1}^{n-2} \frac{|\alpha_i - 2\alpha_{i+1} + \alpha_{i+2}|}{(n-2)}, \quad (4)$$

in which α_i is the V_P (km s^{-1}) of the ith layer and n is the total number of layers. We then plot the roughness value against the corresponding rms residual value for a given inversion. For our synthetic seismogram example, a smoothing parameter is calculated by slightly perturbing the model in Figure 1. The Moho depth is decreased by 5 km, the upper-crustal shear-wave velocity is increased by 2%, the lower crust velocity is decreased by 2%, and the upper-mantle is set to 4.45 km s^{-1}. This perturbed model was then used as the initial model for a series of inversions with gradually increasing smoothing values, and Figure 5 displays the trade-off between waveform fit and resulting model roughness. Selecting a smoothing parameter is marginally subjective, because there is no correct value to employ. We performed inversions using smoothing parameters of 0.05, 0.075, and 0.1, and solution models for our synthetic seismogram example yield results that are all comparable to one another. We select a smoothing parameter of 0.1 because it generates the smoothest solution model that still fits the data properly, and this smoothing parameter is used for all inversions performed with the synthetic seismogram. As mentioned previously, the synthetic seismograms were created without the inclusion of noise, and thus the solution models shown below would be the best case. In the Synthetic Seismogram Inversion section, we assess the robustness of our approach by further performing the inversion with our synthetic seismogram.

Synthetic Seismogram Inversion

We perform an inversion of the upgoing S wavefield shown in Figure 3, using the window size determined from the analysis outlined in Figure 4. The smoothing constraint within the inversion formulation minimizes the second derivative of the velocity with depth. This implies that the velocity model for adjacent layers should obey a linear velocity gradient. This regularization constraint battles with the behavior of the data if there are discrete velocity jumps in the Earth structure. Our philosophy is to apply the smoothing constraint sparingly with the weighting parameter σ, such that any needed velocity discontinuity can develop to model observed *Ps* conversions. The initial models for the inversion are constructed from the ak135 Earth model (Fig. 6; Kennett *et al.*, 1995), in which we fit a smooth curve to the ak135 shear-wave velocity model and perturb the smooth curve by randomly increasing or decreasing the velocity in each layer by up to 0.15 km s^{-1} (Fig. 6). This removes any large velocity contrasts as well as any bias on crustal structure or thickness. In general, the wavelength of a shear-wave traveling through the crust for a frequency of ~0.8 Hz, which is typical for our upgoing S wave, is about 4 km. Therefore, layers as thin as 1 km could potentially influence the solution model assuming *a priori* information is known. However, because we do not include *a priori* information in our initial models, we keep layer thicknesses between 2 and 3 km for our inversion scheme.

All results from the synthetic inversion roughly converge on the same solution (Fig. 7). The resulting models relocate the Moho to ~34 km, which closely matches the Moho depth in Figure 1 (35 km). It is worth highlighting that the model in Figure 1 begins at the surface, whereas results shown in Figure 7 begin at a downward continued depth of 2 km; therefore, the depth to the Moho in Figure 7 may appear shallower than that in Figure 1. The average upper-crustal V_S is ~3.5 km s^{-1}, with an average lower crustal V_S of ~3.8 km s^{-1}, again providing a close match to the model in Figure 1. However, upper-mantle V_S mismatches that of the actual velocity model. As shown in Figure 4, the availability of phases associated with midcrustal discontinuities or the Moho outnumber those from the upper mantle. Furthermore, deeper phase conversions arrive after the S_{Moho} arrival within the ice–Moho reflection reverberations. Because of this, resolution of deeper structures is diminished, due to the masking of their waveforms. The solution models within the upper mantle do, however, closely match the trend of the actual model. The waveform data are also fit

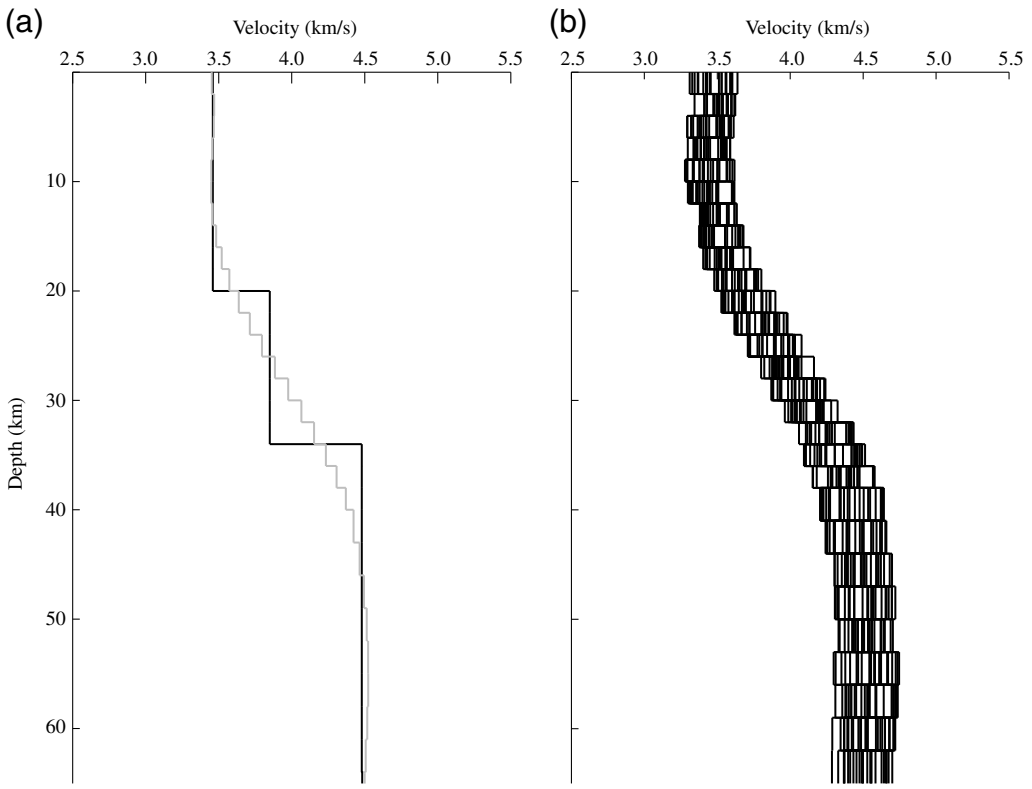

Figure 6. Initial models for synthetic inversion. (a) The smoothed ak135 model is shown in gray, with the original model (Kennett *et al.*, 1995) shown in black, for reference. (b) Perturbations to the smoothed ak135 model shown in (a). Each layer is randomly increased or decreased up to 0.15 km s^{-1}, creating 24 individual perturbed models.

reasonably well (Fig. 7). The inversion of the synthetic seismogram shows that reasonable solution models can be calculated without the constraints of *a priori* information. Large velocity contrasts (i.e., Moho) are imaged in the solution models as well as smaller-scale velocity contrasts in the midcrust and uppermost mantle.

All solutions fit the waveform data equally well (Fig. 7), thereby illustrating the nonuniqueness of the method. This nonuniqueness mirrors that of standard receiver and transfer function inversions in that many solution models are capable of fitting a single waveform (Ammon *et al.*, 1990; Graw *et al.*, 2015), and this is why we present a breadth of results from inversions using 24 slightly different initial models. This displays the quasi-variance in the solution models. We further demonstrate the effectiveness of the method by performing analyses using real datasets from Antarctica.

Inversion of Antarctic Data

To illustrate the practicality of our method for real polar seismic investigations, we now apply our inversion approach to data recorded by stations located on the East and West Antarctic ice sheets. Our analysis will focus on two seismic stations: one that is part of the Transantarctic Mountains Northern Network (Hansen *et al.*, 2015, TAMNNET; station BEBP; Fig. 8) and the other that is part of the Polar Earth Observing Network (POLENET; station WAIS; Fig. 8). We also use data from a small array (Korea Polar Seismic Network [KPSN]) maintained by the Korea Polar Research Institute (Park *et al.*, 2014). Stations BEBP and WAIS were chosen due to their contrasting geological settings. Station BEBP is located on thinner ice compared to station WAIS and was deployed within the cratonic setting of the East Antarctic plateau (Fretwell *et al.*, 2013; Hansen *et al.*, 2014, 2016; Graw *et al.*, 2016; Heeszel *et al.*, 2016). Station WAIS, on the other hand, was deployed within the West Antarctic rift system, which is thought to be underlain by lower upper-mantle velocities and thinner crust compared to that beneath East Antarctica (Chaput *et al.*, 2014; Heeszel *et al.*, 2016; Ramirez *et al.*, 2016). Teleseismic *P* waves from earthquakes with epicentral distances ranging from 30° to 90° are conventionally used in transfer function analyses given their near-vertical incidence angles and the fact that their signals are not generally disturbed by other arriving phases (Langston, 1977, 1979; Helmberger, 1983). Therefore, our dataset is composed of teleseismic events within this distance range, with minimum magnitudes of 6.8. There is no prefiltering applied to the data prior to deconvolution. Additionally, the instrument response is not removed prior to deconvolution. The instrument responses for the stations nearly match one another with small differences in their gains. Therefore, we equalize the gains across all stations prior to analysis.

It should be noted that the success of our method relies heavily upon the geometry at the ice–bedrock interface, because it has been shown that a dipping interface of large

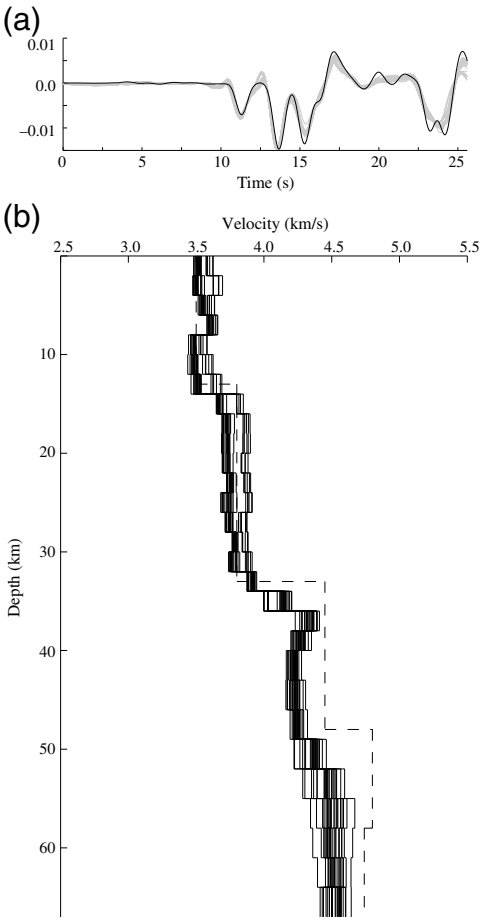

Figure 7. (a) Black line is the windowed upgoing *S* wavefield (Fig. 3), and gray lines show waveform fits from each of the 24 inversion solutions. (b) Resulting solution models from the 24 individual inversions. The dashed line is the actual model from Figure 1.

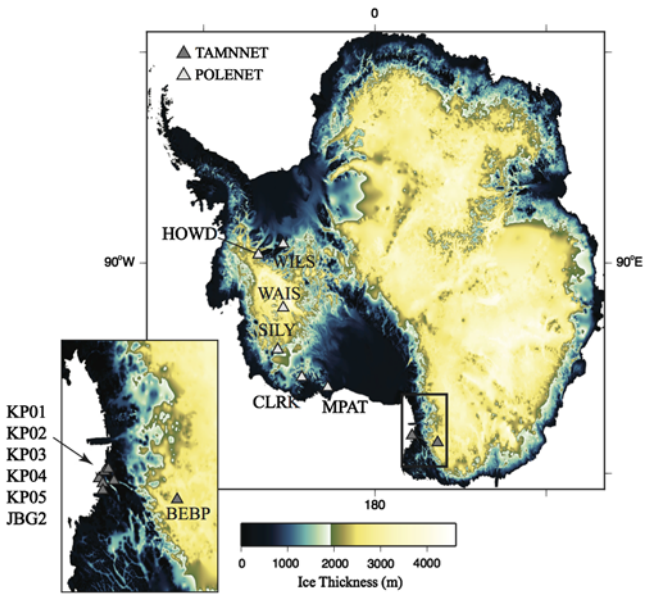

Figure 8. Map showing the locations for all stations (triangles) used in our Antarctic data analysis. Dark gray stations in East Antarctica are associated with the Transantarctic Mountains Northern Network (TAMNNET) analysis, and light gray stations in West Antarctica are associated with the Polar Earth Observing Network (POLENET) analysis. The TAMNNET area highlighted by the black box is magnified in the inset (lower left). Ice thicknesses are from the BEDMAP2 model (Fretwell *et al.*, 2013). The color version of this figure is available only in the electronic edition.

impedance contrast will distort the vertical and radial *P*-wave responses and significantly increase the amplitude of the tangential component (Langston, 1977). However, these effects primarily occur for dips that are greater than ~10° (Langston, 1977). In general, the TAMNNET and POLENET arrays are both located over areas with complex bedrock topography containing many valleys and sub-ice mountain peaks, and careful consideration went into choosing stations for our method. Stations BEBP and WAIS were selected because they reside over areas of relatively simple, gently dipping bedrock topography, thus eliminating the influence of a dipping ice–bedrock interface on our *P*-wave responses. Processing of the data, including deconvolution and downward continuation, would not be possible for stations overlying complex bedrock topography without precise knowledge of the geometry of the ice–bedrock interface and the use of finite-difference techniques.

P-Wave Transfer Function Equalization

To generate our *P*-wave transfer functions, we adopt an approach similar to that developed by Langston and Hammer (2001), in which an array beam of vertical components is deconvolved from the individual station's radial component to construct a radial-component transfer function. This network average of vertical components reduces random scattering effects and stabilizes the entire deconvolution process.

The vertical component of motion is important because it is the sole representation of the source wavelet itself; however, the vertical component is dominated by ice layer reverberations, which mask any remnant of the source wavelet. Because of this, Langston (2011) suggested using vertical-component data from stations situated outside the area overlain by the low-velocity surface layer to obtain the best source time function for deconvolution (i.e., stations located on hard rock). For our Antarctic dataset, we construct an array-averaged vertical component from the KPSN network (stations JBG2, KP01-05) for the TAMNNET data analysis and a similar vertical component from POLENET stations CLRK, HOWD, MPAT, SILY, and WILS to analyze station WAIS (Fig. 8). Each station in the vertical array beam is situated on hard basement rock, thereby creating the best source time function representation for a given teleseismic event.

Deconvolution of the vertical-component array beam from a given station's radial component is performed in the frequency domain through spectral division using a water-level deconvolution technique (Helmberger and Wiggins, 1971). A water-level parameter of 0.01 is used for deconvolution to avoid division by zero. The transform of a Gaussian is applied to the resultant transfer function prior to conversion back to the time domain to filter out any high-frequency random noise. The Gaussian equation is given by

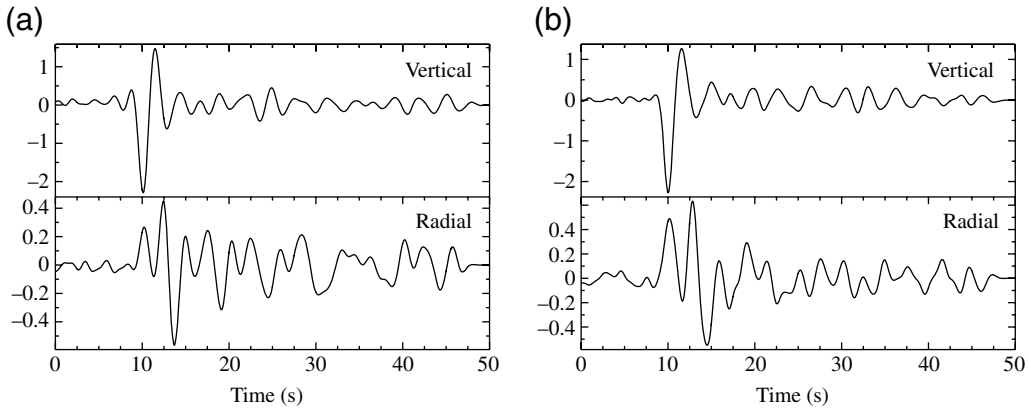

Figure 9. Example (top) vertical and (bottom) radial component transfer functions for stations (a) BEBP and (b) WAIS. Data shown for station BEBP come from the 24 August 2014 event (Table 1), and data shown for station WAIS come from the 12 August 2010 event (Table 2).

$$G(\omega) = e^{\frac{-\omega^2}{4\zeta^2}}, \tag{5}$$

in which ζ is a constant that controls the width of the Gaussian function. Transfer functions were created with ζ values of 1.0, 2.0, and 3.0; however, we chose to proceed with a ζ of 2.0 for both stations BEBP and WAIS because it results in signals with higher retained frequencies and, ultimately, more information within the waveforms (Fig. 9). Ⓔ Figure S1 (available in the electronic supplement to this article) provides an example of the *P*-wave equalization original waveforms (Ⓔ Fig. S1a–c), stack (Ⓔ Fig. S1d), rotated waveforms (Ⓔ Fig. S1e,f), and deconvolution results (Ⓔ Fig. S1g–i). The downward continuation and wavefield decomposition, followed by the inversion of the upgoing *S* wavefield, is performed in an analogous manner as that applied to the synthetic analysis.

Station BEBP: TAMNNET Analysis

We first apply our methodology to data recorded by station BEBP from the TAMNNET array (Fig. 8). Previous studies based on PRFs indicate an ice thickness of 2.75 km beneath this station (Hansen *et al.*, 2016), whereas the BEDMAP2 model (Fretwell *et al.*, 2013) suggests an ice thickness of 2.90 km. Additionally, Hansen *et al.* (2016) computed SRFs for this station and found a mean crustal thickness of 38.5 ± 3.7 km, with an average crustal V_S of 3.70 ± 0.08 km s^{-1}. Upper-mantle V_S was estimated by Graw *et al.* (2016) from surface-wave tomography, who found velocities of ∼4.4 km s^{-1} at depths shallower than 80 km.

Our dataset for station BEBP consists of four events (Table 1), each of which was preprocessed using the criteria described in the *P*-wave Transfer Function Equalization section. All corresponding upgoing *S*-wavefields were stacked into a single trace to increase the SNR prior to inversion. Because the thickness of the surface medium through which the *P* wave is being downward continued must be known, we take the same approach as that used with the synthetic example to calculate the upgoing *P* wavefield, using a variety of models, each with slightly thicker ice layers. Stacks of both the vertical and radial components from the events in Table 1 were used to perform the ice thickness test. The average correlation coefficients for the upgoing *P* wavefields indicate that the ice beneath station BEBP is 2.8 km thick (Fig. 10). This agrees well with previous estimates from Hansen *et al.* (2016; ∼2.75 km) and BEDMAP2 (2.90 km; Fretwell *et al.*, 2013). Given our ice thickness measurement, all data used in the inversion were downward continued to a depth of 2.85 km. Based on our windowing tests (Fig. 4) and crustal-thickness estimates from previous studies, we window the stacked upgoing *S* wavefield from 0 to 28 s prior to inversion.

Similar to our synthetic analysis, we also determine the rms residual versus model roughness using the initial model from the synthetic analysis, and we find that a smoothing value of 0.1 reduces the residual vector while still maintaining a relatively smooth solution model (Fig. 11). This smoothing parameter was used for all successive inversions of the station BEBP data, and all inversions converged within four or five iterations. To avoid any potential bias from previous studies, we use the same 24 initial models associated with our syn-

Table 1
Station BEBP Event Parameters

Date (yyyy/mm/dd)	Time (UTC) (hh:mm:ss.ss)	Latitude (°)	Longitude (°)	Depth (km)	M_w	Distance (°)	BAZ (°)
2013/05/23	17:26:57.00	−23.02	−177.10	171.4	7.4	52.05	30.83
2014/08/24	23:33:19.00	−14.59	−73.57	101	6.8	86.65	131.61
2014/11/01	19:05:14.02	−19.69	−177.75	434	7.1	55.23	29.43
2015/10/20	22:00:45.00	−14.85	167.30	135	7.1	58.47	11.85

BAZ, back azimuth.

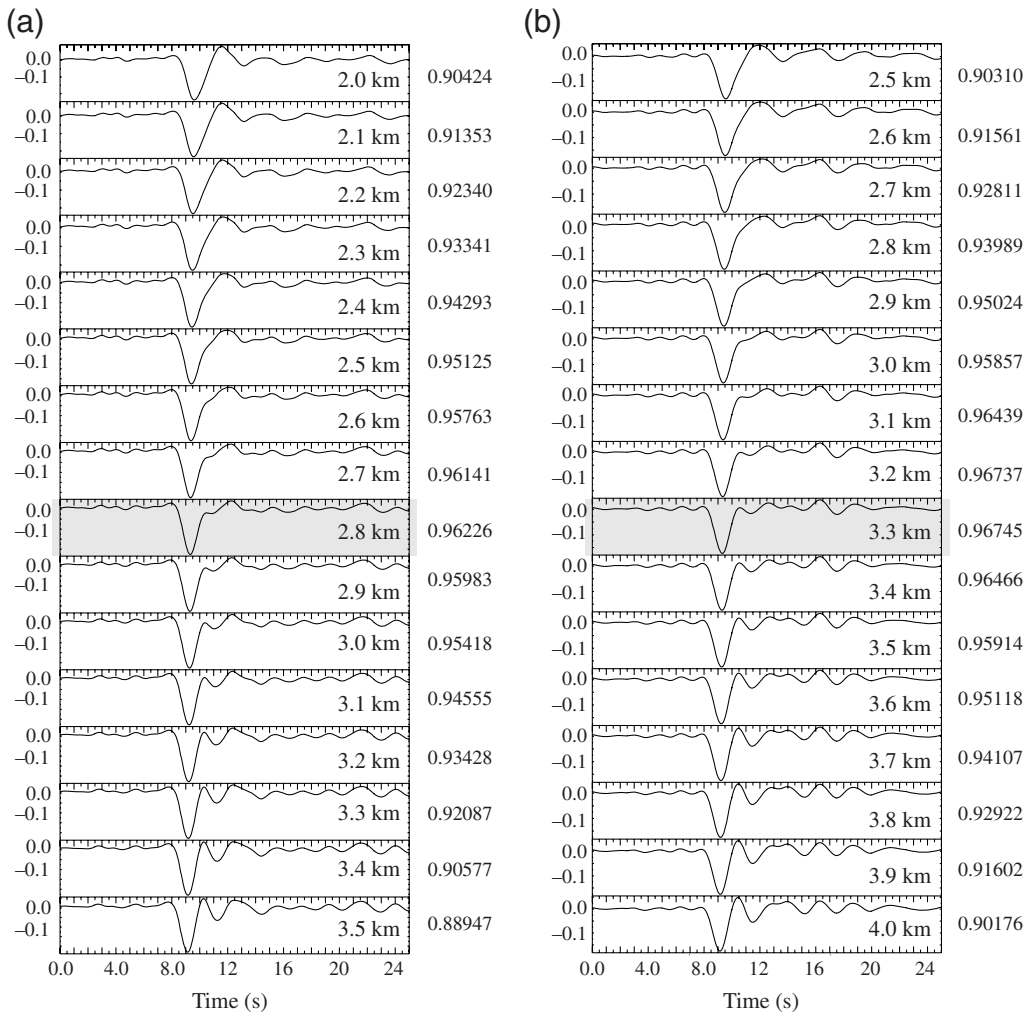

Figure 10. Upgoing *P* wavefields for a series of downward continuation and decomposition tests for stations (a) BEBP and (b) WAIS. The velocity models for each successive calculation are the same, except the ice layer thickness is progressively increased (indicated on the right of each trace). The gray shading indicates the best estimate for ice thickness for each station. Ice thicknesses of 2.8 and 3.3 km best minimize the secondary reflections for stations BEBP and WAIS, respectively. Numbers to the right of each trace are the average maximum correlation coefficient for that upgoing *P* wave when cross correlated with the rest of the upgoing *P* waves, as described in the Downward Continuation and Wavefield Decomposition section.

thetic test (Fig. 6) and invert the upgoing *S* wavefield for station BEBP using each input model. Results from the different inversions are shown in Figure 12. The stacked upgoing *S* wavefield, along with the associated waveform fits from each inversion, are also provided. The solutions indicate a Moho depth of ~38 km, which matches that previously found by SRF analysis (Hansen *et al.*, 2016). Our average crustal V_S ranges from 3.63 to 3.74 km s^{-1}, which also falls within estimates from Hansen *et al.* (2016). Average upper-mantle V_S beneath station BEBP ranges from 4.40 to 4.68 km s^{-1}, coinciding well with the ~4.4 km s^{-1} estimate of upper-mantle velocity from Graw *et al.* (2016). Waveforms from the inversion fit the data well (Fig. 12).

Station WAIS: POLENET Analysis

We also apply our methodology to station WAIS from the POLENET array (Fig. 8). The BEDMAP2 model (Fretwell *et al.*, 2013) indicates an ice thickness beneath this station of 3.37 km. Modeling of PRFs (Chaput *et al.*, 2014) indicates a corresponding crustal thickness of 22.2 ± 2 km, but SRF analysis (Ramirez *et al.*, 2016) instead indicates a crustal thickness of 19 ± 3 km, with an average crustal V_S of ~3.5 km s^{-1}. Heeszel *et al.* (2016), who took a different approach and estimated Moho depth from a Monte Carlo inversion of surface-wave velocities, found a crustal thickness beneath station WAIS of ~27–28 km. This same study also suggests that upper-mantle V_S beneath station WAIS is ~4.4 km s^{-1}; however, sub-Moho (or rather the ~10 km just below the Moho) V_S estimates are much lower, at ~4.15–4.2 km s^{-1} (Heeszel *et al.*, 2016).

The dataset for station WAIS is composed of three events (Table 2), each preprocessed as previously described. Similar to station BEBP, all upgoing *S* wavefields were stacked for station WAIS prior to inversion. An ice thickness estimate

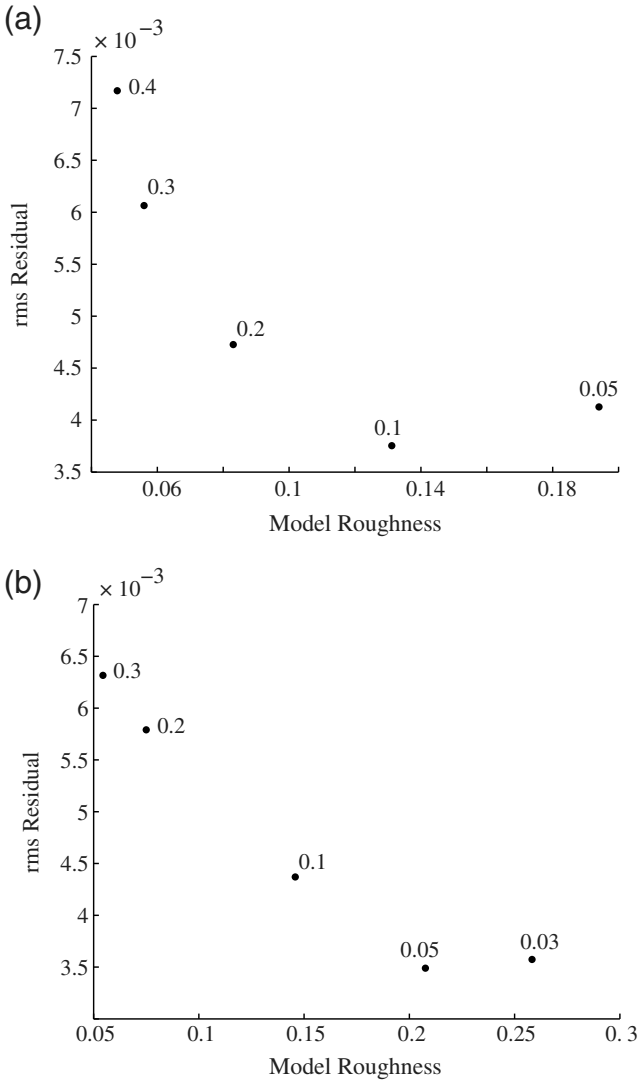

Figure 11. Plots showing the trade-off between waveform fit and model roughness for (a) TAMNNET station BEBP and (b) POLENET station WAIS. Smoothing parameter values are denoted next to each plotted point. For stations BEBP and WAIS, we choose smoothing parameters of 0.1 and 0.05, respectively, for the inversion processes because they reduce the residual vectors while not oversmoothing the solutions.

was again made using the technique demonstrated in our synthetic analysis. A series of upgoing *P* wavefields were examined, and we found an ice thickness of 3.3 km beneath station WAIS, agreeing well with the BEDMAP2 ice thickness estimate (Fig. 10; Fretwell *et al.*, 2013). Given this, the upgoing *S* wavefield was downward continued to a depth of 3.35 km.

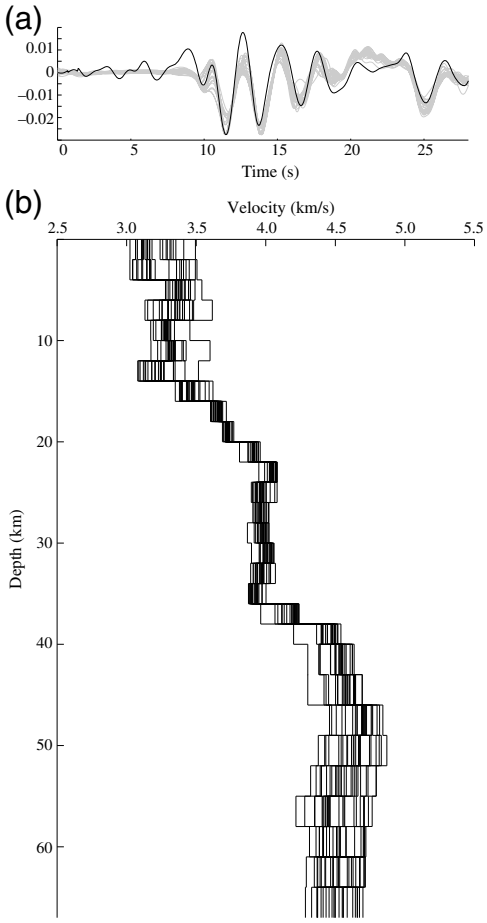

Figure 12. Results from TAMNNET station BEBP. (a) Waveform fits to the data (gray) from each of the 24 inversions. The black line denotes the stacked upgoing *S* wavefield. (b) Resulting solution models for the 24 individual inversions.

Based on our windowing tests (Fig. 4) and crustal thickness estimates from previous studies, we window the stacked upgoing *S* wavefield from 0 to 25 s prior to inversion. As before, a roughness test computation was performed using the initial model from the synthetic analysis to find the best smoothing parameter for the inversion (Fig. 11). We found that a smoothing parameter of 0.05 best minimizes the rms residual vector without resulting in an overly rough model. All inversions performed for station WAIS used this smoothing parameter, and each inversion converged within four or five iterations.

Similar to our TAMNNET analysis, we used the 24 models from our synthetic test (Fig. 6) as the initial inputs for the inversion. This, again, removes any bias for crustal thickness and *a priori* information. Results from the suite of inversions

Table 2
Station WAIS Event Parameters

Date (yyyy/mm/dd)	Time (UTC) (hh:mm:ss.ss)	Latitude (°)	Longitude (°)	Depth (km)	M_w	Distance (°)	BAZ (°)
2010/08/12	12:04:43.00	−1.27	−77.36	206.5	7.1	79.96	35.01
2011/08/24	17:56:32.00	−7.62	−74.53	149.3	7.0	74.01	38.60
2014/08/24	23:31:31.00	−14.59	−73.57	101	6.8	67.24	40.49

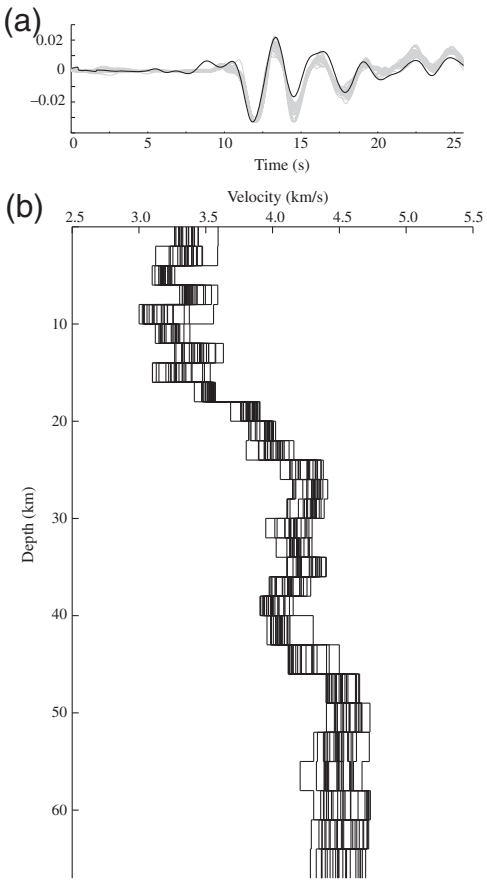

Figure 13. Results from POLENET station WAIS. (a) Waveform fits to the data (gray) from each of the 24 inversions. The black line denotes the stacked upgoing *S* wavefield. (b) Resulting solution models for the 24 individual inversions.

and associated waveform fits are shown in Figure 13. We find a crustal thickness of ∼18 km, which agrees well with results from Ramirez *et al.* (2016), and is within ∼2 km from estimates from Chaput *et al.* (2014). Our assessment of crustal thickness is, however, much thinner than that found by Heeszel *et al.* (2016). Our average crustal V_S values range from 3.48 to 3.63 km s^{-1}, which is in agreement with those determined by the SRF analysis for station WAIS (3.5 km s^{-1}; Ramirez *et al.*, 2016). Our average upper-mantle V_S values range from 4.24 to 4.38 km s^{-1}, which are lower than estimates from Heeszel *et al.* (2016; ∼4.4 km s^{-1}). The lower estimates for mantle velocity could be attributed to anomalously low V_S directly beneath the Moho (Heeszel *et al.*, 2016) influencing the average. Shear-wave velocities deeper than 40 km range from 4.37 to 4.58 km s^{-1}, coinciding with results from the Heeszel *et al.* (2016) study for the upper mantle as a whole.

Data Inversion Summary

Results from the inversion of real polar data indicate that our method resolves high contrast Earth structure within the subsurface. Downward continuation removes reverberations caused by the ice sheet from the transfer functions, and modeling of the resultant upgoing *S* wavefield returns results within the error bounds defined by previous studies, thereby providing confidence in our results. We demonstrated how our method estimates shear-wave velocity structure beneath a given station situated on an ice sheet as well as the usefulness of our approach in acquiring a network-averaged vertical component that can be used as the deconvolution agent to create transfer functions.

Conclusions

Our study showed that the inversion of an upgoing *S* wavefield, generated from a downward-continued and wavefield-decomposed *P* wave, is a feasible method to investigate subsurface structure beneath areas with thick ice coverage. Synthetic tests show that the method is robust, and analyses from real polar seismic data show solution models that agree with results from previous studies. To complement the methodology, a robust calculation for ice thickness is a byproduct of the downward continuation and decomposition process, providing an alternative approach to estimate the thickness of the ice layer when other datasets are unavailable. The relative simplicity of V_P and V_S through an ice medium, combined with the knowledge of ice thickness, hastens the velocity analysis needed for downward continuation, making our method a simple approach to directly study subsurface structure without the need for extensive ice modeling.

Data and Resources

Data management handling was provided by the Incorporated Research Institutions for Seismology (IRIS) Data Management Center (DMC). The software packages Generic Mapping Tools (GMT; Wessel and Smith, 1998) and Seismic Analysis Code (SAC; Goldstein *et al.*, 2003) were used in this study and are gratefully acknowledged.

Acknowledgments

We thank the Transantarctic Mountains Northern Network (TAMNNET), Polar Earth Observing Network (POLENET), and KPSN field teams responsible for maintaining the instrumentation and for collecting the data that have been used in our study, as well as the staff at Incorporated Research Institutions for Seismology (IRIS)-Program for the Array Seismic Studies of the Continental Lithosphere (PASSCAL), Ken Borek Air, and McMurdo Station for their technical and logistical support. We also thank Thomas Brocher, Douglas Wiens, and an anonymous reviewer for their thorough critiques of this article. The facilities of the IRIS Consortium are supported by the National Science Foundation (NSF) under Cooperative Agreement EAR-1063471, the NSF Office of Polar Programs, and the Department of Energy National Nuclear Security Administration. Funding for this project was provided by the NSF (Grant Number ANT-1148982) and by Korean Grant PM15020.

References

Ammon, C. J., G. E. Randall, and G. Zandt (1990). On the nonuniqueness of receiver function inversions, *J. Geophys. Res.* **95,** 15,303–15,318.

Brocher, T. M. (2005). Empirical relations between elastic wavespeeds and density in the Earth's crust, *Bull. Seismol. Soc. Am.* **95,** 2081–2092.

Chaput, J., R. C. Aster, A. Huerta, X. Sun, A. Lloyd, D. Wiens, A. Nyblade, S. Anandakrishnan, J. P. Winberry, and T. Wilson (2014). The crustal thickness of West Antarctica, *J. Geophys. Res.* **119,** 1–18.

Fretwell, P., H. D. Pritchard, D. G. Vaughan, J. L. Bamber, N. E. Barrand, R. Bell, C. Bianchi, R. G. Bingham, D. D. Blankenship, G. Casassa, *et al.* (2013). Bedmap2: Improved ice bed, surface and thickness datasets for Antarctica, *Cryosphere* **7,** 375–393.

Goldstein, P., D. Dodge, M. Firpo, and L. Minner (2003). SAC2000: Signal processing and analysis tools for seismologists and engineers, in *Invited Contribution to IASPEI International Handbook of Earthquake and Engineering Seismology,* W. H. K. Lee, H. Kanamori, P. C. Jennings, and C. Kisslinger (Editors), Academic Press, London, United Kingdom, 1000 pp.

Graw, J. H., A. N. Adams, S. E. Hansen, D. A. Wiens, L. Hackworth, and Y. Park (2016). Upper mantle shear wave velocity structure beneath northern Victoria Land, Antarctica: Volcanism and uplift in the northern Transantarctic Mountains, *Earth Planet. Sci. Lett.* **449,** 48–60, doi: 10.1016/j.epsl.2016.05.026.

Graw, J. H., C. A. Powell, and C. A. Langston (2015). Crustal and upper mantle velocity structure in the vicinity of the eastern Tennessee seismic zone based upon radial *P*-wave transfer functions, *J. Geophys. Res.* **120,** no. 1, 243–258, doi: 10.1002/2014JB011516.

Hansen, S. E., J. H. Graw, L. M. Kenyon, A. A. Nyblade, D. A. Wiens, R. C. Aster, A. D. Huerta, S. Anandakrishnan, and T. Wilson (2014). Imaging the Antarctic mantle using adaptively parameterized *P*-wave tomography: Evidence for heterogeneous structure beneath West Antarctica, *Earth Planet. Sci. Lett.* **408,** 66–78.

Hansen, S. E., J. Julia, A. A. Nyblade, M. L. Pyle, D. A. Wiens, and S. Anandakrishnan (2009). Using *S* wave receiver functions to estimate crustal structure beneath ice sheets: An application to the Transantarctic Mountains and East Antarctic craton, *Geochem. Geophys. Geosys.* **10,** no. Q08014, doi: 10.1029/2009GC002576.

Hansen, S. E., L. M. Kenyon, J. H. Graw, Y. Park, and A. Nyblade (2016). Crustal structure beneath the northern Transantarctic Mountains and Wilkes subglacial basin: Implications for tectonic origins, *J. Geophys. Res.* **121,** no. 2, 812–825, doi: 10.1002/2015JB012325.

Hansen, S. E., A. A. Nyblade, D. S. Heeszel, D. A. Wiens, P. Shore, and M. Kanao (2010). Crustal structure of the Gamburtsev Mountains, East Antarctica, from *S*-wave receiver functions and Rayleigh wave phase velocities, *Earth Planet. Sci. Lett.* **300,** 395–401.

Hansen, S. E., A. M. Reusch, T. Parker, D. K. Bloomquist, P. Carpenter, J. H. Graw, and G. R. Brenn (2015). The Transantarctic Mountains Northern Network (TAMNNET): Deployment and performance of a seismic array in Antarctica, *Seismol. Res. Lett.* **86,** no. 6, 1636–1644, doi: 10.1785/0220150117.

Haskell, N. A. (1962). Crustal reflection of plane *P* and *SV* waves, *J. Geophys. Res.* **67,** 4751–4767.

Heeszel, D. S., D. A. Wiens, S. Anandakrishnan, R. C. Aster, I. W. D. Dalziel, A. D. Adams, A. A. Nyblade, T. J. Wilson, and P. Winberry (2016). Upper mantle structure of central and West Antarctica from array analysis of Rayleigh wave phase velocities, *J. Geophys. Res.* **121,** no. 3, 1758–1775, doi: 10.1002/2015JB012616.

Helmberger, D. V. (1983). Theory and application of synthetic seismograms, in *Earthquakes: Observations, Theory and Interpretation*, H. Kanamori and E. Boschi (Editors), North Holland for the Italian Physical Society, Amsterdam, The Netherlands, 612 pp.

Helmberger, D. V., and R. Wiggins (1971). Upper mantle structure of Midwestern United States, *J. Geophys. Res.* **76,** 3229–3245.

Kennett, B. L. N., E. R. Engdahl, and R. Buland (1995). Constraints on seismic velocities in the Earth from traveltimes, *Geophys. J. Int.* **122,** 108–124.

Kohnen, H. (1974). The temperature dependence of seismic waves in ice, *J. Glaciol.* **13,** 144–147.

Kumar, P., R. Kind, W. Hanka, K. Wylegalla, Ch. Reigber, X. Yuan, I. Woelbern, P. Schwintzer, K. Fleming, T. Dahl-Jensen, *et al.* (2005). The lithosphere–asthenosphere boundary in the north-west Atlantic region, *Earth Planet. Sci. Lett.* **236,** 249–257.

Langston, C. A. (1977). The effect of planar dipping structure on source and receiver responses for constant ray parameter, *Bull. Seismol. Soc. Am.* **67,** 1029–1050.

Langston, C. A. (1979). Structure under Mount Rainier, Washington, inferred from teleseismic body waves, *J. Geophys. Res.* **84,** 4749–4762.

Langston, C. A. (2011). Wave-field continuation and decomposition for passive seismic imaging under deep unconsolidated sediments, *Bull. Seismol. Soc. Am.* **101,** 2176–2190.

Langston, C. A., and J. K. Hammer (2001). The vertical component *P*-wave receiver function, *Bull. Seismol. Soc. Am.* **91,** 1805–1819.

Park, Y., H. J. Yoo, W. S. Lee, J. Lee, Y. Kim, S. Lee, D. Shin, and H. Park (2014). Deployment and performance of a broadband seismic network near the new Korean Jang Bogo Research Station, Terra Nova Bay, East Antarctica, *Seismol. Res. Lett.* **85,** no. 6, 1341–1347, doi: 10.1785/0220140107.

Ramirez, C., A. Nyblade, S. E. Hansen, D. A. Wiens, S. Anandakrishnan, R. C. Aster, A. D. Huerta, P. Shore, and T. Wilson (2016). Crustal and upper-mantle structure beneath ice-covered regions in Antarctica from *S*-wave receiver functions and implications for heat flow, *Geophys. J. Int.* **204,** 1636–1648.

Wessel, P., and W. H. F. Smith (1998). New, improved version of Generic Mapping Tools released, *Eos Trans. AGU* **79,** 579.

Department of Geological Sciences
The University of Alabama
Box 870338
Tuscaloosa, Alabama 35487
jhgraw@crimson.ua.edu
shansen@geo.ua.edu
(J.H.G., S.E.H.)

Center for Earthquake Research and Information
The University of Memphis
3890 Central Avenue
Memphis, Tennessee 38152
clangstn@memphis.edu
(C.A.L.)

Sandia National Laboratory
P.O. Box 5800
Albuquerque, New Mexico 87185
byoung@sandia.gov
(B.A.Y.)

IRIS PASSCAL Instrument Center
New Mexico Institute of Mining and Technology
801 Leroy Place
Socorro, New Mexico 87801
akram@passcal.nmt.edu
(A.M.)

Korea Polar Research Institute
26 Songdomirae-ro, Yeonsu-gu
Incheon 406-840, South Korea
ypark@kopri.re.kr
(Y.P.)

Manuscript received 16 August 2016;
Published Online 21 February 2017